Robotica (2025), **43**, pp. 4005–4021
doi:10.1017/S0263574725102804

CAMBRIDGE UNIVERSITY PRESS

RESEARCH ARTICLE

A comparative analysis of initial-pose self-calibration algorithms for underactuated cable-driven parallel robots

Filippo Zoffoli, Edoardo Idà and Marco Carricato

Department of Industrial Engineering, University of Bologna, Bologna 40137, Italy
Corresponding author: Edoardo Idà; Email: edoardo.ida2@unibo.it

Received: 3 April 2025; **Revised:** 22 July 2025; **Accepted:** 4 October 2025; **First published online:** 27 October 2025

Keywords: cable-driven parallel robots; underactuated robots; initial-pose calibration; self-calibration; nonlinear optimization

Abstract

Underactuated Cable-Driven Parallel Robots (*UACDPRs*) typically rely on relative internal sensors to estimate the end-effector (*EE*) state. Therefore, at startup, the reference values of the quantities measured by these sensors are unknown, and so is the initial pose of the *EE*. The problem of determining the reference values of the internal sensors is called initial-pose self-calibration. The latter is often formulated as an overdetermined system of nonlinear equations and solved using nonlinear weighted least-squares methods, minimizing the error between modeled and measured variables, and its effectiveness is highly influenced by the choice of measurement configurations, as well as the motion planning and control strategy used to reach them. This work presents two practical data acquisition methods for initial-pose self-calibration of *UACDPRs*, aiming to reduce the overall time required by the procedure and enhance process automation. The first method is slower but richer in data, as it relies on equilibrium poses and, therefore, can leverage cable-tension data, whereas the second method is faster and is based on geometric constraints only. The performance of the methods is evaluated in terms of acquisition time, number of measurements, and calibration accuracy on a 4-cable *UACDPR* prototype. The results highlight the merits and shortcomings of both methods, namely, trade-offs between the velocity of data collection and the precision of pose estimation.

1. Introduction

Cable-Driven Parallel Robots (*CDPRs*) are a class of parallel manipulators that utilize cables instead of rigid links to control the pose of the end-effector (*EE*). Each cable is spooled by a drum, which is part of a winch, typically mounted on an external rigid frame. The cable is routed from the drum to the *EE* through a pulley transmission system, where the final pulley is typically designed to swivel around an axis tangent to its groove, ensuring smooth guidance to the robot *EE*. By adjusting the cable lengths via servo-controlled winches, the *EE* can follow a desired trajectory and execute manipulation tasks. Cables exhibit a high payload-to-weight ratio since they are subjected only to tensile stresses, making *CDPRs* both lightweight and capable of handling significant loads [1]. Another key advantage is the ease of deployment and reconfiguration. Indeed, the cable exit points from the frame can be changed online to adapt the *CDPR* workspace to the task to be executed [2, 3] or to minimize power consumption [4]. Alternatively, in the design phase, the *CDPR* geometry can be chosen to maximize stiffness [5], minimize the maximum cable tension [6], or increase dexterity [7]. As cables impose unilateral constraints, *CDPRs* are usually equipped with more cables than the *EE* degrees of freedom (*DOFs*). In this configuration, if all cables always remain taut, the robot is overconstrained. Some *CDPRs*, called Underactuated *CDPRs* (*UACDPRs*), employ fewer cables than the *EE* degrees of freedom [8], and they are inherently underconstrained. Consequently, the *EE* retains some *DOFs* even when all actuators are locked, and the *EE* pose cannot be assessed through direct kinematics only, since infinite poses are

associated with the same set of cable lengths. Compared to overconstrained architectures, *UACDPRs* may offer specific advantages, depending on the application. For example, they improve obstacle avoidance, as fewer cables reduce the risk of interference with the environment, and fixed and operational costs decrease, as fewer actuators are required [9].

Although reconfigurability makes *CDPRs* highly adaptable to varying tasks and environments, frequent reconfigurations present a major challenge: the need for frequent recalibration. At every reconfiguration, a calibration of the robot is needed to accurately determine the changes in the geometric (and possibly the inertial) model parameters, with the aim of enhancing the robot's performance. Geometric calibration involves estimating the robot's parameters by (i) performing some controlled motion of the *EE* to measure some internal variables and a ground truth (i.e., the robot pose) and (ii) minimizing the difference between the ground truth and its mathematical model (which explicitly depends on the measured internal variables) [10]. The conventional approach relies on external sensors to provide the ground truth, such as laser trackers [11], which provide direct measurements of the *EE* pose relative to a fixed reference frame. In this case, the function to be minimized is the difference between measured and modeled *EE* poses [11]. Alternatively, when no additional sensors other than the ones embedded in the robot kinematic chains are used for data acquisition, the procedure is called self-calibration, and it may be preferred to the conventional one, as it requires no additional cost for external sensors. A drawback is that calibration poses must be estimated alongside the robot's geometric parameters. As a result, the number of unknowns increases while the number of independent equations remains the same. This generally reduces the accuracy of the estimated parameters, yielding poorer calibration results.

In *CDPRs*, most authors assume that direct or indirect measures of cable lengths and cable tensions are necessary for controlling the robot, as the former are used to derive motor setpoints, and the latter provide at least additional safety or additional capabilities to the robot. Typically, relative rotary encoders in the winch motors and load cells within the transmission are employed [12]. To compensate for cable elongation and provide a direct measure of cable length, laser distance sensors may also be used [13]. Additionally, incremental encoders can be employed to measure the swivel angles in swivel pulleys [14]. For a direct measure of the *EE* orientation, an Attitude and Heading Reference System (*AHRS*) can be integrated into the platform, thus improving pose estimation accuracy [15, 16]. Finally, cable orientations can be estimated using accelerometers mounted on cables near their anchor points on the platform [17].

Using relative sensors requires performing a procedure at every *CDPR* startup to determine their absolute reference values. This process, too, can be formulated as a self-calibration problem since it is equivalent to determining the initial pose of the *EE* and using the inverse geometric or static problem to determine the sensors' reference values in the said pose.

In the past, several methods were proposed for the initial-pose self-calibration. Typically, the procedure is conducted offline using zero-order kinematics to model cable lengths based on the unknown calibration poses, measuring cable length variations, and minimizing the residuals [11, 18, 19]. Some approaches enhance accuracy by incorporating the swivel-pulley transmission model [20] or leveraging swivel-angle measurements [14]. More recent techniques exploit observability indices to enable online data selection for self-calibration [21, 22]. The initial-pose self-calibration is usually formulated as a Nonlinear Least Squares [14, 18–20] or Nonlinear Weighted Least Squares (*NWLS*) [11, 21, 22] problem, where the unknowns include the initial values of the relative sensors and the measurement poses. The residual vector is composed of the difference between the quantities modeled by inverse kinematics (in the case of cable lengths or swivel angles) or statics (for cable tensions) and the measured ones. Even though effective solutions have been proposed for solving the initial-pose self-calibration problem of *UACDPRs* from a theoretical standpoint, there is still room for improvement in both accuracy and calibration speed. Current state-of-the-art methods require several minutes for automatic data acquisition [14], and the initial estimated pose exhibits position and orientation errors of 2.5 cm and 2.2 degrees, respectively [23].

This paper extends the work presented in [23], where a rapid method for data acquisition and initial-pose self-calibration was introduced. This method aims at reducing data acquisition time, maintaining

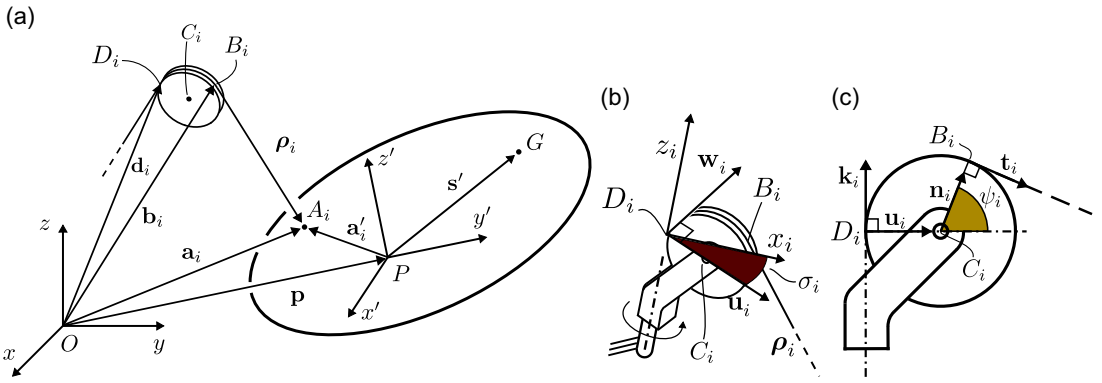

Geometric model of a cable transmission | Swivel-pulley | Swivel pulley plane

Figure 1. *UACDPR geometric model.*

the same accuracy for the resulting initial pose compared to previous studies [14]. While [23] achieved significant improvements in data acquisition efficiency, it requires operator intervention. In this study, we propose two novel data acquisition algorithms aimed at increasing the degree of automation while maintaining rapid and accurate self-calibration:

1. The first method involves moving the robot to static equilibrium poses, ensuring taut cables via low-level tension control, similarly to [14]. Swivel-angle and cable-length variations are measured using incremental encoders, while an *AHRS* mounted on the *EE* captures orientation data. Load cells are used to measure cable tensions and regulate the motion of the *UACDPR*.
2. The second method solely relies on geometric constraints for self-calibration. It employs the same set of sensors as the first method but excludes load-cell measurements, using them only for *EE* motion control.

In both cases, the initial-pose estimation problem is formulated as a *NWLS* optimization problem, where the residuals to be minimized are the differences between the model-predicted values and actual sensor measurements. Experimental validation is conducted on a 4-cable *UACDPR* prototype, demonstrating the proposed methods' effectiveness in reducing calibration time while maintaining accuracy.

The remainder of the paper is organized as follows. Section 2 introduces the kinematic and static models of a *UACDPR*. Section 3 presents the proposed self-calibration methodology, including data acquisition procedures. The experimental validation of the method on a 4-cable *UACDPR* is described in Section 4. Finally, conclusions and future research are provided in Section 5.

2. Kinematic and static models

A spatial *UACDPR* with a 6-degree-of-freedom (*DoF*) *EE* and n cables is considered, with $n < 6$. Cables are assumed to be massless and inextensible; therefore, no sagging or elastic phenomena are considered, and cables can be modeled as straight lines. This assumption is reasonable for small-scale *UACDPRs*, where the cable mass is negligible compared to the *EE* mass, and elastic deformations have a minimal effect on system behavior [24]. Indicating the inertial frame with $Oxyz$ and the frame attached to the *EE* with $Px'y'z'$, the *EE* pose is defined by the position vector $\mathbf{p}$ of P and the rotation matrix $\mathbf{R}(\boldsymbol{\epsilon})$, where $\boldsymbol{\epsilon} = [\phi\ \theta\ \chi]^T$ contains the Euler angles according to the *ZYX* convention. Consequently, the generalized coordinates of the *EE* are $\boldsymbol{\zeta} = [\mathbf{p}^T\ \boldsymbol{\epsilon}^T]^T$. Each cable is guided by a swiveling pulley into the workspace (Figure 1a). The i-th cable enters the pulley groove at the fixed point D_i, exits at B_i, and is anchored to the platform at point A_i. To express the position of B_i in the inertial frame, we introduce a local reference

frame $D_i x_i y_i z_i$, with constant unit vectors $\mathbf{i}_i$, $\mathbf{j}_i$, $\mathbf{k}_i$ (Figure 1b and 1c). The pulley geometry is modeled as in [23]. Each pulley of radius r_i and center C_i is tangent to the local axis z_i at D_i and swivels about z_i by the angle σ_i. If the unit vector $\mathbf{u}_i$ points from D_i to C_i, and the unit vector $\mathbf{w}_i$ is orthogonal to the pulley groove plane, then $\mathbf{w}_i = \mathbf{k}_i \times \mathbf{u}_i$. The tangency angle ψ_i defines the orientation of the unit vector $\mathbf{n}_i$, which points from C_i to B_i. The unit vector along the i-th cable is $\mathbf{t}_i = \mathbf{w}_i \times \mathbf{n}_i$. The aforementioned unit vectors can be described as:

$$\begin{aligned} \mathbf{u}_i &= \cos\sigma_i \mathbf{i}_i + \sin\sigma_i \mathbf{j}_i, \qquad & \mathbf{w}_i &= -\sin\sigma_i \mathbf{i}_i + \cos\sigma_i \mathbf{j}_i, \\ \mathbf{n}_i &= \cos\psi_i \mathbf{u}_i + \sin\psi_i \mathbf{k}_i, \qquad & \mathbf{t}_i &= \sin\psi_i \mathbf{u}_i - \cos\psi_i \mathbf{k}_i. \end{aligned} \tag{1}$$

The position of D_i in the inertial frame $Oxyz$ is identified by the constant vector $\mathbf{d}_i$, while B_i is described by $\mathbf{b}_i = \mathbf{d}_i + r_i(\mathbf{u}_i + \mathbf{n}_i)$. The constant position of A_i in the local frame $Px'y'z'$ is denoted by ${}^P\mathbf{a}'_i$, and in $Oxyz$ is given by $\mathbf{a}_i = \mathbf{p} + \mathbf{a}'_i = \mathbf{p} + \mathbf{R}\,{}^P\mathbf{a}'_i$. Defining the vector $\boldsymbol{\varrho}_i = A_i - D_i = \mathbf{a}_i - \mathbf{d}_i$, and assuming that the cable remains coplanar with the swivel pulley, the resulting constraint is $\mathbf{w}_i \cdot \boldsymbol{\varrho}_i = 0$. From the latter, the swivel angle is found through inverse kinematics as:

$$\sigma_i = \operatorname{atan2}(\mathbf{j}_i \cdot \boldsymbol{\varrho}_i, \mathbf{i}_i \cdot \boldsymbol{\varrho}_i). \tag{2}$$

Then, defining the cable vector as $\boldsymbol{\rho}_i = A_i - B_i$, and considering pulley kinematics, we obtain:

$$\boldsymbol{\rho}_i = \mathbf{a}_i - \mathbf{b}_i = \boldsymbol{\varrho}_i - r_i(\mathbf{u}_i + \mathbf{n}_i). \tag{3}$$

Since the cable is tangent to the pulley groove in B_i, the tangency angle ψ_i is determined using the geometric constraint $\mathbf{n}_i \cdot \boldsymbol{\rho}_i = 0$, leading to:

$$\psi_i = 2\arctan\left(\frac{\varrho_{k_i}}{\varrho_{u_i}} + \sqrt{\left(\frac{\varrho_{k_i}}{\varrho_{u_i}}\right)^2 + 1 - \frac{2r_i}{\varrho_{u_i}}}\right), \tag{4}$$

where $\varrho_{k_i} = \boldsymbol{\varrho}_i \cdot \mathbf{k}_i$ and $\varrho_{u_i} = \boldsymbol{\varrho}_i \cdot \mathbf{u}_i$. The total cable length $l_i\ (>0)$ consists of the rectilinear segment $\|\boldsymbol{\rho}_i\|$ and the arc $\widehat{D_i B_i}$ wrapped around the pulley:

$$l_i = \|\boldsymbol{\rho}_i\| + r_i(\pi - \psi_i). \tag{5}$$

The *CDPR* static model is obtained from the mechanical equilibrium of the *EE*. The model is formulated under the assumption that all cables remain taut and that gravity is the only external force acting on the *EE*, so that:

$$\boldsymbol{\Xi}^T \boldsymbol{\tau} = \mathbf{f}, \quad \text{with} \quad \mathbf{f} = \begin{bmatrix} \mathbf{g} \\ \mathbf{s}' \times \mathbf{g} \end{bmatrix}, \tag{6}$$

where $\mathbf{g} = [0, 0, -mg]^T$, m is the *EE* mass, g is the gravitational acceleration, $\mathbf{s}'$ is the position vector from P to the center of mass G, and $\boldsymbol{\tau} \in \mathbb{R}^n$ is the array of cable tensions. $\boldsymbol{\Xi}^T \in \mathbb{R}^{6\times n}$ is the structure matrix, which relates cable tensions to forces and torques on the *EE*, and is computed as in [25]:

$$\boldsymbol{\xi}_i = \begin{bmatrix} \mathbf{t}_i \\ \mathbf{a}'_i \times \mathbf{t}_i \end{bmatrix}, \qquad \boldsymbol{\Xi}^T = [\boldsymbol{\xi}_1, \ldots, \boldsymbol{\xi}_n]. \tag{7}$$

3. Self-calibration and data-acquisition algorithms

In previous studies [11, 18–20], motor encoders have been used as primary sensors for *CDPR* self-calibration. For overconstrained *CDPRs*, load cells have been shown to be effective for this purpose too [26, 27].

In this work, as in [23], we consider *UACDPRs* equipped with multiple internal sensors for state estimation and motion control. In particular, indicating the measured quantities with the superscript $(\cdot)^*$, an incremental encoder on the i-th swivel pulley measures variations in the swivel angles $\Delta\sigma_i^*$ relative to the angular position at startup $\sigma_{i,0}$. An *AHRS*, rigidly attached to the platform with its reference

frame coincident with the *EE* mobile frame, provides roll and pitch angles (ϕ^* and θ^*) relative to a local-earth frame (east-north-up) coinciding with *Oxyz*, as well as the relative yaw variation $\Delta\chi^*$ from the startup configuration χ_0. Additionally, an incremental encoder in the winch motor tracks the motor angle displacement $\Delta\theta^*_{m,i}$ relative to the startup value $\theta_{m,i,0}$. When the i-th winch is designed with a constant and known transmission ratio K between cable-length variation and motor displacement (as assumed here), the cable-length variation can be indirectly estimated as $\Delta l^*_i = K\Delta\theta^*_{m,i}$ [28]. Finally, a load cell is integrated into each transmission to measure the i-th cable tension τ^*_i.

The choice of this sensor set is based on three main reasons. First, previous studies [15, 16] demonstrated the effectiveness of incremental encoders and *AHRSs* for accurate pose estimation in *UACDPRs*. Therefore, it is reasonable to adopt this configuration as the available internal sensor suite, since these sensors will also be used for state estimation after calibration. Second, cable-tension measurements, whether obtained directly through load cells or estimated from motor currents [29], are typically employed for control and safety purposes, such as ensuring that all cables remain taut during operation. Since these measurements are already available in the control loop, they can be naturally included in the self-calibration formulation to enhance pose estimation accuracy. Third, the use of multiple sensors helps mitigate errors introduced by the simplified modeling assumptions described in Section 2, where cables are modeled as straight lines and the swivel pulleys are assumed to remain coplanar with the corresponding cable directions.

If other internal sensing systems are available, such as laser distance sensors for directly measuring cable elongation [13], they can be easily integrated into our approach, which is fully general. Indeed, including additional sensors may yield faster and more accurate results.

3.1. Self-calibration algorithms

At a generic *EE* pose $\boldsymbol{\zeta}_i$, if the constraints imposed by the swivel pulleys and the cables on the moving platform are active,[1] the relationships between modeled and measured quantities for cable lengths, swivel angles, and orientation angles can be expressed as:

$$\mathbf{l}(\boldsymbol{\zeta}_i) = \mathbf{l}_0 + \Delta\mathbf{l}^*_i, \quad \boldsymbol{\sigma}(\boldsymbol{\zeta}_i) = \boldsymbol{\sigma}_0 + \Delta\boldsymbol{\sigma}^*_i, \tag{8}$$

$$\phi(\boldsymbol{\zeta}_i) = \phi^*_i, \quad \theta(\boldsymbol{\zeta}_i) = \theta^*_i, \quad \chi(\boldsymbol{\zeta}_i) = \boldsymbol{\chi}_0 + \Delta\chi^*_i. \tag{9}$$

In Eqs. (8) and (9), the modeled cable-length array $\mathbf{l}(\boldsymbol{\zeta}_i)$ and swivel-angle array $\boldsymbol{\sigma}(\boldsymbol{\zeta}_i)$ are obtained through inverse kinematics, namely through Eqs. (5) and (2), whereas the modeled Euler angles $\phi(\boldsymbol{\zeta}_i)$, $\theta(\boldsymbol{\zeta}_i)$, and $\chi(\boldsymbol{\zeta}_i)$ are the orientation components of the pose $\boldsymbol{\zeta}_i$. The measured quantities in Eqs. (8) and (9), instead, depend on the directly measured data $\Delta\mathbf{l}^*$, $\Delta\boldsymbol{\sigma}^*$, ϕ^*, θ^*, $\Delta\chi^*$ and on the initial values $\mathbf{l}_0$, $\boldsymbol{\sigma}_0$, χ_0.

Additionally, if the generic pose $\boldsymbol{\zeta}_i$ is a static equilibrium one, the relation between the modeled and measured cable tensions is given by:

$$\boldsymbol{\tau}(\boldsymbol{\zeta}_i) = \boldsymbol{\tau}^*_i, \tag{10}$$

where the modeled tension array $\boldsymbol{\tau}(\boldsymbol{\zeta}_i)$ can be computed from (6) through a generic left inverse $\boldsymbol{\Xi}^{-T}$ of the structure matrix:

$$\boldsymbol{\tau}(\boldsymbol{\zeta}_i) = \boldsymbol{\Xi}^{-T}(\boldsymbol{\zeta}_i)\mathbf{f}(\boldsymbol{\zeta}_i). \tag{11}$$

To define a specific inverse of $\boldsymbol{\Xi}^T$, we partition it into two blocks, namely $\boldsymbol{\Xi}^T = [\boldsymbol{\Xi}_c \; \boldsymbol{\Xi}_f]^T$, where $\boldsymbol{\Xi}_c \in \mathbb{R}^{n\times n}$ and $\boldsymbol{\Xi}_f \in \mathbb{R}^{n\times(6-n)}$. The corresponding left inverse is given by:

[1] Due to the unilateral nature of cable actuation, the constraints imposed by the swivel pulleys and cable lengths hold only when cables remain taut and tension forces are sufficient to overcome pulley friction. Under these conditions, the cable vectors remain coplanar with the pulley planes, ensuring the validity of pulley constraints.

$$\boldsymbol{\Xi}^{-T} = \left[\boldsymbol{\Xi}_c^{-T}\ \mathbf{0}_{n\times(6-n)}\right], \tag{12}$$

where $\mathbf{0}_{n\times(6-n)}$ is a null matrix with n rows and $(6-n)$ columns.

In conventional formulations (e.g., [11, 14, 18–20, 22]), the array of unknowns $\mathbf{X}$ in the initial-pose self-calibration problem, typically includes the initial values $\mathbf{l}_0$, $\boldsymbol{\sigma}_0$, χ_0, as well as multiple measurement poses $\mathbf{Z} = [\boldsymbol{\zeta}_1^T, \ldots, \boldsymbol{\zeta}_k^T]^T$. With a sufficient number of measurement poses k, an overdetermined nonlinear system of equations composed by Eqs. (8), (9), and (10) can be established, which is desirable to reduce the impact of measurement errors. In contrast, in our approach, the initial values $\mathbf{l}_0$, $\boldsymbol{\sigma}_0$, and χ_0 are reformulated as explicit functions of the initial *EE* pose $\boldsymbol{\zeta}_0$, using the kinematic relations in Eqs. (5) and (2). This reformulation shifts the estimation task from identifying the initial value of the measured quantities to estimating the initial *EE* pose (together with the measurement poses). The residuals for the i-th measurement equilibrium pose become:

$$\begin{aligned} \mathbf{F}_{\tau,i} &= \boldsymbol{\tau}(\boldsymbol{\zeta}_i) - \boldsymbol{\tau}_i^*, \\ \mathbf{F}_{l,i} &= \mathbf{l}(\boldsymbol{\zeta}_i) - \mathbf{l}_0(\boldsymbol{\zeta}_0) - \Delta\mathbf{l}_i^*, \\ \mathbf{F}_{\sigma,i} &= \boldsymbol{\sigma}(\boldsymbol{\zeta}_i) - \boldsymbol{\sigma}_0(\boldsymbol{\zeta}_0) - \Delta\boldsymbol{\sigma}_i^*, \end{aligned} \qquad \mathbf{F}_{\epsilon,i} = \begin{bmatrix} \phi(\boldsymbol{\zeta}_i) - \phi_i^* \\ \theta(\boldsymbol{\zeta}_i) - \theta_i^* \\ \chi(\boldsymbol{\zeta}_i) - \chi_0(\boldsymbol{\zeta}_0) - \Delta\chi_i^* \end{bmatrix} \tag{13}$$

Therefore, the actual calibration task becomes the estimation of $\boldsymbol{\zeta}_0$, from which the initial values of the measured quantities can be derived via inverse kinematics. This strategy reduces the number of unknowns and thus increases the equation-to-unknown ratio. Assuming that the modeling error introduced by inverse kinematics is negligible, this leads to improved computational efficiency and fewer measurements to obtain a desired accuracy in the estimation. Therefore, the same approach as in [23] is used, where the array of unknowns $\mathbf{X} = [\boldsymbol{\zeta}_0^T, \boldsymbol{\zeta}_1^T, \ldots, \boldsymbol{\zeta}_k^T]^T \in \mathbb{R}^{6(k+1)}$ is composed by the initial pose $\boldsymbol{\zeta}_0$ and k measurement configurations.

Two self-calibration algorithms are considered, each utilizing a different sensor set and indexed by $j \in \{\tau l\sigma\epsilon, l\sigma\epsilon\}$. The first algorithm ($j = \tau l\sigma\epsilon$) uses all the available sensors, including those measuring cable tensions, swivel-angle variations, cable-length variations, roll, pitch, and yaw variations. The second algorithm ($j = l\sigma\epsilon$) excludes cable tension measurements and only relies on the other sensors. The motivation for considering these two algorithms lies in the set of equations available for the self-calibration process, which directly influences the data acquisition strategy. On the one hand, maximizing the ratio between the number of equations and the number of unknowns is desirable, and this can be achieved by incorporating all available sensors, including load cells. However, using load cell measurements inherently requires relying on static equilibrium equations, as dynamic equations would introduce additional unknowns (namely, pose derivatives), counteracting the goal of maximizing the equation-to-unknowns ratio. As a consequence, the calibration process must rely on static *EE* poses, potentially leading to longer data acquisition times due to the need for self-energy dissipation. Excluding load cell measurements simplifies the calibration process by relying only on geometric constraints, as shown in [23]. This allows for rapid movements and faster data acquisition at the cost of a lower equation-to-unknowns ratio, which may, in turn, reduce the accuracy of calibration results.

In both algorithms, the initial-pose self-calibration problem is formulated as a *NWLS* optimization:

$$\mathbf{X}_{sol,j} = \arg\min_{\mathbf{X}} h_j(\mathbf{X}), \quad \text{with} \quad h_j(\mathbf{X}) = \frac{1}{2}\mathbf{F}_j^T\mathbf{W}_j\mathbf{F}_j. \tag{14}$$

The residual array $\mathbf{F}_j$ is composed of different combinations of residual blocks depending on the sensor set used :

$$\mathbf{F}_{\tau l\sigma\epsilon} = [\mathbf{F}_\tau^T\ \mathbf{F}_l^T\ \mathbf{F}_\sigma^T\ \mathbf{F}_\epsilon^T]^T \in \mathbb{R}^{k(3n+3)}, \qquad \mathbf{F}_{l\sigma\epsilon} = [\mathbf{F}_l^T\ \mathbf{F}_\sigma^T\ \mathbf{F}_\epsilon^T]^T \in \mathbb{R}^{k(2n+3)}. \tag{15}$$

Each residual block is constructed by vertically stacking the corresponding single-pose residuals defined in Eq. (13) across all k measurement configurations:

$$\mathbf{F}_\sigma = \begin{bmatrix} \boldsymbol{\sigma}(\boldsymbol{\zeta}_1) - \boldsymbol{\sigma}_0(\boldsymbol{\zeta}_0) - \Delta\boldsymbol{\sigma}_1^* \\ \vdots \\ \boldsymbol{\sigma}(\boldsymbol{\zeta}_k) - \boldsymbol{\sigma}_0(\boldsymbol{\zeta}_0) - \Delta\boldsymbol{\sigma}_k^* \end{bmatrix} \in \mathbb{R}^{kn}, \; \mathbf{F}_\epsilon = \begin{bmatrix} \phi(\boldsymbol{\zeta}_1) - \phi_1^* \\ \theta(\boldsymbol{\zeta}_1) - \theta_1^* \\ \chi(\boldsymbol{\zeta}_1) - \chi_0(\boldsymbol{\zeta}_0) - \Delta\chi_1^* \\ \vdots \\ \phi(\boldsymbol{\zeta}_k) - \phi_k^* \\ \theta(\boldsymbol{\zeta}_k) - \theta_k^* \\ \chi(\boldsymbol{\zeta}_k) - \chi_0(\boldsymbol{\zeta}_0) - \Delta\chi_k^* \end{bmatrix} \in \mathbb{R}^{3k},$$

$$\mathbf{F}_l = \begin{bmatrix} \mathbf{l}(\boldsymbol{\zeta}_1) - \mathbf{l}_0(\boldsymbol{\zeta}_0) - \Delta\mathbf{l}_1^* \\ \vdots \\ \mathbf{l}(\boldsymbol{\zeta}_k) - \mathbf{l}_0(\boldsymbol{\zeta}_0) - \Delta\mathbf{l}_k^* \end{bmatrix} \in \mathbb{R}^{kn}, \qquad \mathbf{F}_\tau = \begin{bmatrix} \boldsymbol{\tau}(\boldsymbol{\zeta}_1) - \boldsymbol{\tau}_1^* \\ \vdots \\ \boldsymbol{\tau}(\boldsymbol{\zeta}_k) - \boldsymbol{\tau}_k^* \end{bmatrix} \in \mathbb{R}^{kn}. \tag{16}$$

In the *NWLS* formulation (14), the residual vector $\mathbf{F}_j$ contains components of heterogeneous nature, each with different units and levels of reliability. To account for this and to normalize the residual contributions in the cost function, a weighting matrix $\mathbf{W}_j$ is introduced. We assume that the residuals are uncorrelated and that their associated errors, comprising both measurement noise and model uncertainty, can be approximated as zero-mean white Gaussian noise. Under these assumptions, and following standard estimation theory [30], the optimal weighting matrix is diagonal, with each diagonal element equal to the inverse of the variance of the corresponding residual component. Following the practical implementation adopted in [16], the variances are approximated using the maximum expected errors of each measurement signal, accounting for both sensor specifications and known model uncertainties. This leads to the following definition:

$$\mathbf{W}_{\tau l \sigma \epsilon} = \text{diag}\left(\left[\frac{1}{\delta\tau_{max}^2}\cdot\mathbf{1}_{1\times nk}, \frac{1}{\delta l_{max}^2}\cdot\mathbf{1}_{1\times nk}, \frac{1}{\delta\sigma_{max}^2}\cdot\mathbf{1}_{1\times nk}, \frac{1}{\delta\epsilon_{max}^2}\cdot\mathbf{1}_{1\times 3k}\right]\right),$$

$$\mathbf{W}_{l\sigma\epsilon} = \text{diag}\left(\left[\frac{1}{\delta l_{max}^2}\cdot\mathbf{1}_{1\times nk}, \frac{1}{\delta\sigma_{max}^2}\cdot\mathbf{1}_{1\times nk}, \frac{1}{\delta\epsilon_{max}^2}\cdot\mathbf{1}_{1\times 3k}\right]\right), \tag{17}$$

where $\mathbf{1}$ denotes an array of ones. The terms $\delta\tau_{max}, \delta l_{max}, \delta\sigma_{max}, \delta\epsilon_{max}$ represent the maximum expected errors (standard deviations) of the respective measurements, estimated according to the procedure described in [16]. Using these values ensures that each residual contributes proportionally to the overall cost, leading to an unbiased and balanced estimation of the unknowns $\mathbf{X}_{sol}$.

3.2. Data acquisition

The first objective of the data-acquisition methods presented in this work is to ensure well-distributed measurement poses within the static workspace of the robot [8]. This helps condition the numerical solution to the nonlinear problem in Eq. (14), thus increasing the likelihood of convergence from an initial pose guess to the actual initial pose. The second objective is to define a control strategy and motion planning approach to move the *EE* to the measurement poses while satisfying the following requirements:

1. the motion control cannot rely on sensor reference values, as they are unknown at startup (their determination is the goal of the algorithm) or affected by high uncertainties;
2. in spite of requirement 1, the control strategy has to bring the *UACDPR* close enough to some ideal pre-determined measurement poses;
3. motion planning and control must keep tension within a lower and an upper bound, to prevent slackness and avoid cable breakage or exceeding actuator torque limits;

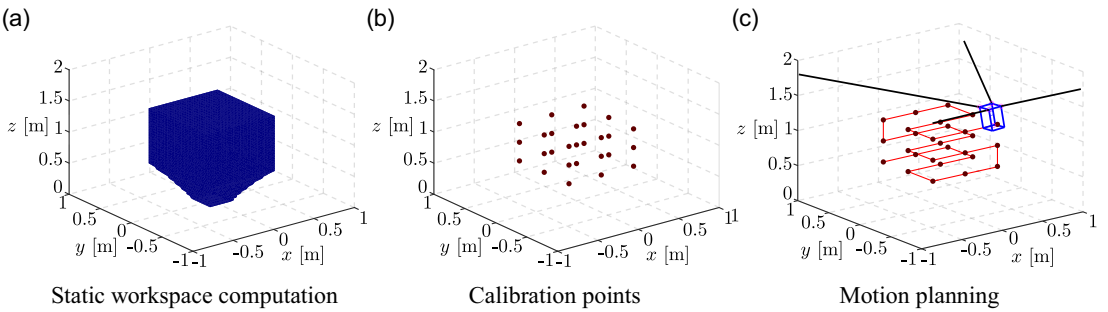

Figure 2. *Calibration poses selection and control planning.*

4. since the first calibration method relies on static equations, the *EE* must be brought to equilibrium configurations, reducing residual oscillations and enabling rapid data acquisition.

3.2.1. Selection of the measurement poses

Numerous theoretical methods have been proposed to determine optimal measurement configurations for calibration based on observability indices [31]. These approaches include discrete optimization over a predefined set of poses [32, 33], introducing deviations from ideal poses for improved robustness [34], and online iterative pose selection to maximize observability [22]. However, the direct application of these methods is challenging, since most of them assume that the robot can reach any *EE* pose, which is true for overconstrained *CDPRs* (e.g., [33, 34]) and, more generally, for non-underactuated architectures [31, 32]. In contrast, *UACDPRs* can only partially control the *EE* pose due to inherent actuation limitations [35], so that observability criteria for fully actuated systems must be adapted, which is beyond the scope of this paper. For this reason, we adopt a more pragmatic, heuristic-based strategy.

For the method involving static equations, we select equispaced positions along the Cartesian axes within the workspace to ensure a uniform distribution of calibration configurations. This approach adapts the methodology originally proposed in [26] for overconstrained *CDPRs*, which ensures that measurement poses are well distributed in space and leads to a well-conditioned *NWLS* problem. To implement this approach, we first evaluate the robot's static workspace to determine its feasible boundaries. This is achieved using the method proposed in [8], which involves discretizing the 3D installation volume with a grid of candidate points $\mathbf{p}_j$ for $j = 1, \ldots, N$. Each point $\mathbf{p}_j$ is tested for inclusion in the static workspace by solving the inverse geometrico-static problem, which provides the complete equilibrium pose and corresponding cable tensions for a given position. Wrench feasibility and equilibrium stability are then checked to validate the configuration. The overall boundary of the static workspace is finally reconstructed using the alpha-shape algorithm [36], based on the collection of valid points (see Figure 2a). The complete algorithm for checking if a point belongs to the static workspace is detailed in Appendix A.

Once the static workspace is defined, we select translational bounds $\mathbf{p}_{lb}$ and $\mathbf{p}_{ub}$ that define the corners of a parallelepiped inscribed in the static workspace. A regular grid of n_x, n_y, and n_z points is computed across the position intervals $[\mathbf{p}_{lb,x}, \mathbf{p}_{ub,x}]$, $[\mathbf{p}_{lb,y}, \mathbf{p}_{ub,y}]$, and $[\mathbf{p}_{lb,z}, \mathbf{p}_{ub,z}]$. Figure 2b shows an example with $n_x = n_y = n_z = 3$. At each position, we apply the method detailed in Appendix A to solve the inverse geometrico-static problem and determine the orientation that satisfies static equilibrium. The resulting k_s poses are stored in the array $\mathbf{Z}_{ideal}$, and their associated cable tensions, computed using Eq. (A2), are stored as future control setpoints in the matrix $\mathbf{T}_{setpoint} = [\boldsymbol{\tau}_1, \ldots, \boldsymbol{\tau}_{k_s}]$. This procedure ensures that each measurement pose corresponds to a valid and controllable static equilibrium.

For the second self-calibration method, which does not rely on static equilibrium, we apply a similar principle in the time domain. Constant-velocity trajectories are executed across the workspace, and data are sampled at uniform time intervals. This approach aims to approximate a uniform spatial distribution of measurement poses. Although it does not explicitly optimize observability indices, prior studies

suggest that calibration can still be effective if the poses are sufficiently numerous and well distributed in the workspace [37, 38]. Observability-based pose selection maximizes the sensitivity of the residuals to the unknown parameters, which improves convergence when only a limited number of poses is used. However, comparable results may be achieved using a sufficient number of uniformly or randomly sampled configurations, particularly near workspace boundaries [32]. Therefore, the proposed approach offers a pragmatic solution that can ensure acceptable accuracy, provided that the control strategy maintains the kinematic constraints (i.e., cable tensions remain within the prescribed bounds).

3.2.2. Data-acquisition procedure

Recalling requirements 1 through 4, it is not feasible to move the *EE* between equilibrium measurement poses and simultaneously suppress residual oscillations using conventional trajectory shaping techniques for vibration damping, such as input-shaped trajectories (e.g., [35]). These methods require accurate joint-position feedback, which in turn depends on a calibrated reference for cable lengths. Therefore, they are only applicable after the initial self-calibration process has been completed.

Furthermore, robust control strategies for *UACDPRs* that can cope with large geometric uncertainties (such as those present prior to calibration) remain an open research challenge. For this reason, a conservative control approach was adopted in this study, prioritizing safety and constraint preservation performance.

Once the static equilibrium measurement poses are defined and the *UACDPR* is powered on, joint-space force control is used to drive the *EE*. Assuming that the *EE* starts within the static workspace, the initial cable tensions are recorded, and a smooth transition is commanded toward a desired tension vector $\boldsymbol{\tau}_0$. In this context, we define $\hat{\boldsymbol{\tau}}(t)$ as the time-varying tension reference used to guide the *EE* between each equilibrium configuration $\boldsymbol{\tau}_i \in \mathbf{T}_{setpoint}$.[2] While any static configuration corresponding to $\boldsymbol{\tau}_0$ is theoretically valid, a convenient "home" pose may be chosen, and $\boldsymbol{\tau}_0$ accordingly computed via static analysis. This initial motion is essential for generating the initial guess used in Section 3.3.

After allowing sufficient time for the *EE* to reach equilibrium, data logging begins. The tension setpoints in $\mathbf{T}_{setpoint}$ are then sequentially applied, with a waiting period introduced after each setpoint $\boldsymbol{\tau}_i$ is reached. Static equilibrium at each pose is detected by monitoring the ripple in the measured cable tensions. When the amplitude of the ripple falls below the load cell's uncertainty threshold, the system is considered to have reached a steady state, and residual oscillations are assumed to be negligible.

The sequence of equilibrium poses is chosen to minimize transition time (Figure 2c). Although there is no explicit control of the *EE* pose between tension setpoints, pure force control maintains active cable constraints, ensuring requirement 3 is met. Since this method is sensitive to load-cell noise, accurate calibration of load cells is crucial. If the measured cable tensions deviate from their true value, the actual equilibrium configurations of the *EE* may differ from the expected ones, leading to incorrect assumptions about static constraints. This, in turn, may affect the accuracy of the self-calibration algorithm, as the constraints used to estimate the initial pose may no longer be valid. Moreover, unaccounted tension errors can lead to situations where the *EE* moves outside the static workspace, further compromising the reliability of the collected measurements.

To minimize total data acquisition time, we adopted a trial-and-error approach to tune the trajectory profiles, striking a balance between fast transitions (enabled by higher velocities) and short oscillation damping periods. This tuning process is architecture-specific and needs to be performed only once for a given *UACDPR*. If the system's geometric and inertial properties remain unchanged, the identified motion parameters can be reused across all subsequent startups, ensuring that the proposed self-calibration procedure remains fully automatic in routine operation. This assumption aligns with the

[2]In this work, a 5th-degree polynomial is used to generate each cable-tension setpoint. This approach does not guarantee that the *EE* remains strictly inside the static workspace during transitions, but the motion profiles can be experimentally adjusted to keep constraints active (e.g., by increasing the transition duration).

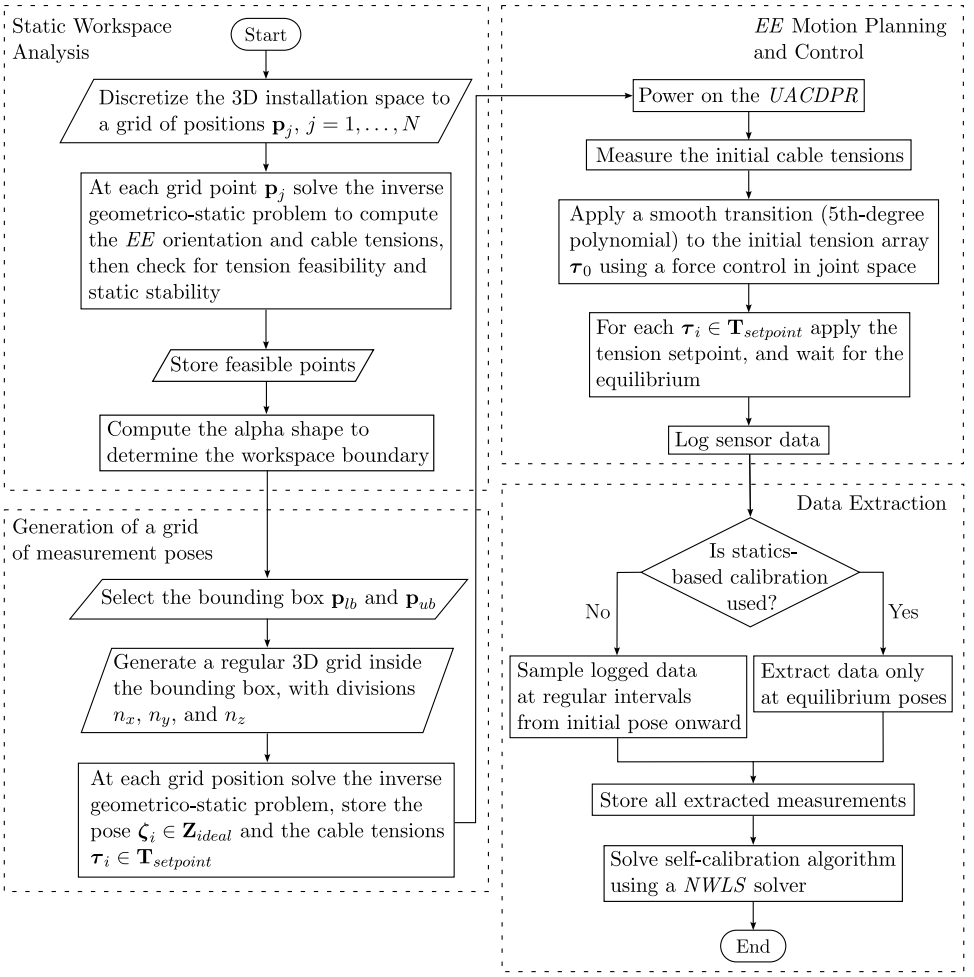

Figure 3. *Flowchart of the data-acquisition algorithm.*

current objective of automating initial-pose self-calibration, which is based on a fixed mechanical architecture. However, it would need to be reconsidered if the method were extended to the self-calibration of geometric parameters, as might be required in reconfigurable *UACDPRs*.

The data acquisition method for the two self-calibration algorithms described in Section 3.1 differs in the data extraction procedure. For the static-equation-based method, only equilibrium pose measurements from $\mathbf{Z}_{ideal}$ are used, identified by the stationary values of measured tensions in the pre-defined setpoints $\mathbf{T}_{setpoint}$. In contrast, for the method that does not rely on static equations, since Eqs. (8) and (9) are valid during the entire data acquisition procedure, any measure following the one corresponding to the initial pose is a valid candidate for the calibration measurement set. Therefore, any sample time that is a multiple of the logging interval can be selected to collect a sufficient number of measurements k and to uniformly distribute measurement poses in the workspace.

The complete acquisition workflow for both self-calibration strategies is summarized in the flowchart in Figure 3.

3.3. Initial guess

The self-calibration problem (14) is solved using a gradient-based optimizer, whose convergence depends on the quality of the initial guess $\mathbf{X}_{guess} = [\boldsymbol{\zeta}_{0,guess}^T, \mathbf{Z}_{guess}^T]^T$. For both self-calibration algorithms,

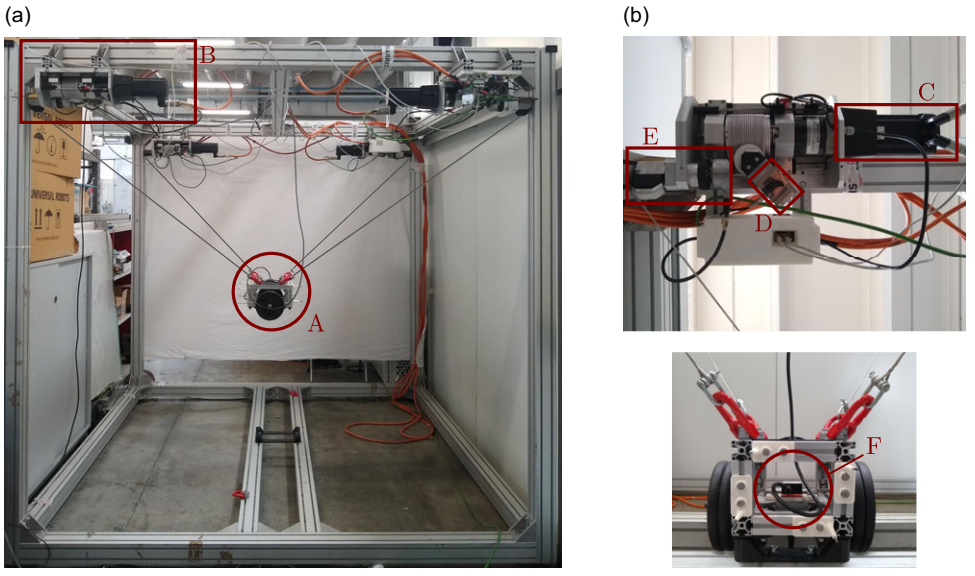

UACDPR prototype setup Winch and platform particulars

Figure 4. *Extperimental setup.*

the initial guess for the pose $\boldsymbol{\zeta}_{0,guess}$ is obtained by solving the direct static problem (6) using the given tension setpoint $\boldsymbol{\tau}_0$. For the measurement poses comprised in the array $\mathbf{Z}_{guess}$, a suitable tentative solution for the self-calibration algorithm with $j = \tau l \sigma \epsilon$ is given by the ideal equilibrium poses included in the array $\mathbf{Z}_{ideal}$. For the self-calibration with $j = l \sigma \epsilon$, instead, the procedure for finding a suitable initial tentative solution is taken from [23]:

1. from the initial equilibrium pose $\boldsymbol{\zeta}_{0,guess}$, cable lengths $\mathbf{l}_{0,guess}$ and swivel angles $\boldsymbol{\sigma}_{0,guess}$ are obtained through inverse kinematics;
2. estimates of cable lengths $\mathbf{l}_i^*$ and swivel angles $\boldsymbol{\sigma}_i^*$ relative to the i-th measurement pose are obtained by adding the i-th cable-length variations and swivel-angle variations measured during the *EE* motion to $\mathbf{l}_{0,guess}$ and $\sigma_{0,guess}$, namely $\mathbf{l}_i^* = \mathbf{l}_{0,guess} + \Delta\mathbf{l}_i^*$ and $\boldsymbol{\sigma}_i^* = \boldsymbol{\sigma}_{0,guess} + \Delta\boldsymbol{\sigma}_i^*$; this computation is made for all measurement poses, thus obtaining $\mathbf{l}_i^*, \ldots, \mathbf{l}_k^*$ and $\boldsymbol{\sigma}_i^*, \ldots, \boldsymbol{\sigma}_k^*$;
3. the measurement pose vector $\mathbf{Z}_{guess}$ is obtained performing a pose estimation for each measurement pose using the corresponding reference values of $\mathbf{l}_i^*$, $\boldsymbol{\sigma}_i^*$, and $\boldsymbol{\epsilon}_i^*$, through the sensor-fusion algorithm described in [16].

4. Experiments and results

The effectiveness of the data acquisition method presented in Section 3.2 was assessed through experiments on a spatial 4-cable UACDPR prototype at the IRMA L@B laboratory of the University of Bologna, shown in Figure 4. The self-calibration algorithms described in Section 3.1 were tested offline in a MATLAB environment. Table I reports the constant geometric parameters of the *UACDPR*, where **i**, **j**, and **k** are the unit vectors of the local pulley frames aligned with the *Oxyz* axes. The coordinates of vectors $\mathbf{d}_i$ and ${}^P\mathbf{a}_i'$ are expressed in *Oxyz* and *Pxyz*, respectively. These values were measured using a meter tool with an uncertainty of 1 mm. The *EE* mass, measured with a weighing scale, is $m = 12.992$ kg, and the vector that points from P to G, obtained by the CAD model of the platform and expressed in the mobile frame, is ${}^P\mathbf{s}' = [0\,0\,0.173]^T$ m. The sensors employed are shown in Figure 4b, where the platform (A in Figure 4a) and the winch (B in Figure 4a) are shown in detail. Specifically, cable lengths

Table I. *Geometrical parameters of the 4-cable UACDPR prototype.*

i	r_i[m]	$\mathbf{d}_i$[m]	${}^P\mathbf{a}'_i$[m]	x_i	y_i	z_i
1	0.03	$[1.065\ -1.155\ 1.839]^T$	$[0.075\ -0.075\ 0.266]^T$	$-\mathbf{k}$	$\mathbf{j}$	$\mathbf{i}$
2	0.03	$[1.066\ 1.155\ 1.839]^T$	$[0.075\ 0.075\ 0.266]^T$	$-\mathbf{k}$	$\mathbf{j}$	$\mathbf{i}$
3	0.03	$[-1.066\ 1.155\ 1.839]^T$	$[-0.075\ 0.075\ 0.266]^T$	$-\mathbf{k}$	$-\mathbf{j}$	$-\mathbf{i}$
4	0.03	$[-1.065\ -1.155\ 1.839]^T$	$[-0.075\ -0.075\ 0.266]^T$	$-\mathbf{k}$	$-\mathbf{j}$	$-\mathbf{i}$

were estimated by using 20-bit incremental encoders with an uncertainty of $\pm 0.144^\circ$ on each motor axis (C in Figure 4b), whereas swivel angles were measured by 16-bit incremental encoders with an uncertainty of $\pm 0.03^\circ$ (E in Figure 4b), mounted directly on the swivel axes of pulleys. Cable tensions were measured using load cells inside the transmission (D in Figure 4b) with a full scale (*F.S.*) of 100 kg, and accuracy of 0.02% *F.S. EE* Euler angles (*ZYX* convention) were measured using an *Xsens MTi-630 AHRS* fixed to the platform (F in Figure 4b). The uncertainty is $\pm 0.2^\circ$ for roll and pitch and $\pm 1^\circ$ for yaw. The *AHRS* was configured to set the startup value of the yaw measure to 0, as the north reference value given by the magnetometer is not reliable due to the high electro-magnetic disturbances in the *UACDPR* environment. The maximum absolute noise levels, based on the aforementioned sensor specifications and on unmodeled effects were estimated according to the results of [16] as:

$$|\delta\sigma_{max}| = 1^\circ, \quad |\delta l_{max}| = 0.01\ \text{m}, \quad |\delta\epsilon_{max}| = 2^\circ, \quad |\delta\tau_{max}| = 10\ \text{N}. \tag{18}$$

To measure the real *EE* initial pose $\boldsymbol{\zeta}_{0,real} = [\mathbf{p}^T_{0,real}\ \boldsymbol{\epsilon}^T_{0,real}]^T$ and use it as ground truth for the self-calibration results, a manual homing procedure was performed before each test. The platform was positioned against a mechanical support where the nominal values of cable lengths, swivel angles, and yaw were previously measured with a high-precision photogrammetry system.

After the static workspace analysis, the translational bounds were set as:

$$\mathbf{p}_{lb} = \begin{bmatrix} -0.4 & -0.4 & 0.6 \end{bmatrix}^T \text{m} \quad \text{and} \quad \mathbf{p}_{ub} = \begin{bmatrix} 0.4 & 0.4 & 1.2 \end{bmatrix}^T \text{m}. \tag{19}$$

The choice of the number of measurement poses k was guided by the main objective of this work: achieving automatic self-calibration in reduced time, without compromising accuracy. For the same reason, our evaluation is mainly based on the calibration time. To analyze the effect of different measurement-pose sets on the initial-pose self-calibration, two spatial grids were discretized using different values of n_x, n_y, and n_z. In the first grid, $n_x = n_y = n_z = 2$, resulting in a total of $k = 8$ equilibrium poses. In the second grid, $n_x = n_y = n_z = 3$, yielding $k = 27$ poses. The equilibrium poses $\mathbf{Z}_{ideal}$ and tension setpoints $\mathbf{T}_{setpoint}$ for $k = 2$ are reported in Table II as an example, while results for $k = 27$ are omitted as they do not provide additional insights.

The initial tension setpoint was set close to the first component $\boldsymbol{\tau}_1$ of $\mathbf{T}_{setpoint}$ (which is the same for the two grids), at $\boldsymbol{\tau}_0 = [100.00\ 100.00\ 100.00\ 100.00]$ N. The data logging rate for all sensors was 100 ms, balancing file size and data resolution. The self-calibration problem (14) was solved using a PC with a 13th generation Intel i7 processor and 32 GB of RAM, distributing the computation across 14 cores. For both $j = \tau l \sigma \epsilon$ and $j = l \sigma \epsilon$ the *fmincon* MATLAB routine with a trust-region-reflective algorithm was used with a termination tolerance of 10^{-10} on the function value, of 10^{-8} on the first-order optimality, and of 10^{-10} on the optimization variables. The gradient was analytically formulated to improve computational efficiency, as in [23], and the initial guess was generated using the methods described in Section 3.3. A graphical representation of the measured tensions, along with the reference trajectory $\hat{\boldsymbol{\tau}}$ used to transition between the equilibrium configurations, is shown in Figure 5.

The results of the two self-calibration methods introduced in Section 3.1 are reported in Table III, where the following data are specified:

Table II. *Ideal measurement poses and tension setpoints, with* $n_x = n_y = n_z = 2$.

i	$\boldsymbol{\zeta}_{ideal,i}$ [m, rad]	$\boldsymbol{\tau}_{setpoint,i}$ [n]
1	$[0.40\ 0.40\ 1.20\ 0.08\ -0.09\ 0.01]^T$	$[118.48\ 170.83\ 115.57\ 82.98]^T$
2	$[-0.40\ 0.40\ 1.20\ 0.08\ 0.09\ -0.00]^T$	$[82.98\ 115.57\ 170.83\ 118.48]^T$
3	$[-0.40\ -0.40\ 1.20\ -0.08\ 0.09\ 0.00]^T$	$[115.49\ 82.97\ 118.54\ 170.73]^T$
4	$[0.40\ -0.40\ 1.20\ -0.08\ -0.09\ -0.00]^T$	$[170.73\ 118.54\ 82.97\ 115.49]^T$
5	$[0.40\ -0.40\ 0.60\ -0.15\ -0.15\ -0.01]^T$	$[81.18\ 55.90\ 31.01\ 53.86]^T$
6	$[-0.40\ -0.40\ 0.60\ -0.15\ 0.15\ 0.01]^T$	$[53.86\ 70.04\ 81.18\ 31.01]^T$
7	$[-0.40\ 0.40\ 0.60\ 0.15\ 0.15\ -0.01]^T$	$[31.01\ 53.87\ 81.21\ 55.87]^T$
8	$[0.40\ 0.40\ 0.60\ 0.15\ -0.15\ 0.01]^T$	$[55.87\ 81.21\ 53.87\ 31.01]^T$

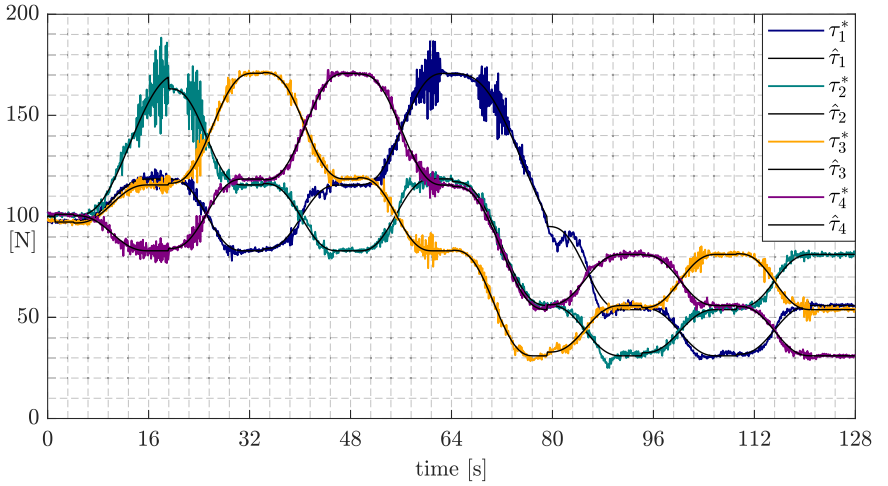

Figure 5. *Sampled and reference tensions with* $k = 8$. *The black curves, with superscript* ($\hat{}$), *represent the tension reference applied during transitions, while the colored curves are the measured tensions, with superscript* (*).

- the used sensor set j, and thus, the related self-calibration algorithm;
- the total self-calibration time t_{sc}, composed by the data acquisition time and initial-pose estimation time;
- the number of pose measurements k used in the algorithm;
- the resulting initial position error norm $\varepsilon_p = \|\mathbf{p}_{0,real} - \mathbf{p}_{0,sol}\|$;
- the resulting initial orientation error $\varepsilon_r = |\alpha_{0,real} - \alpha_{0,sol}|$, where α_0 is the rotation angle in the axis-angle parameterization of the initial orientation. The angle α is obtained from the rotation matrix $\mathbf{R}(\boldsymbol{\epsilon})$ as:

$$\alpha = \arccos\left(\frac{\mathbf{R}_{1,1}(\epsilon) + \mathbf{R}_{2,2}(\epsilon) + \mathbf{R}_{3,3}(\epsilon) - 1}{2}\right). \tag{20}$$

Trials a and b share the same dataset, corresponding to the data acquisition in which the *EE* transitioned between 8 equilibrium poses. Similarly, trials c and d share a dataset where the *EE* followed the path with 27 equilibrium poses. Therefore, the data acquisition time for trials a and b is the same and equal to $t_{da} = 2.13$ min, whereas $t_{da} = 5.11$ min for trials c and d. The total self-calibration time t_{sc} reported in Table III consists of both the data acquisition time t_{da} and the computational time required by the solver t_{opt}, which depends on the number of poses k used in the optimization. For trials b and d,

Table III. *Initial-pose self-calibration algorithm results.*

Trial	j	t_{sc} [min]	k	ε_p [mm]	ε_r [deg]
a	$\tau l \sigma \epsilon$	2.23	8	12	1.24
b	$l \sigma \epsilon$	2.24	19	23	5.44
c	$\tau l \sigma \epsilon$	10.04	27	7.2	3.14
d	$l \sigma \epsilon$	10.02	128	22	2.86

where cable tension measurements were not used, the pose sampling rate from the logged dataset was chosen such that the number of extracted poses k yielded an optimization time t_{opt} approximately equal to that of their tension-based counterparts (trials a and c). This ensured a fair comparison between methods that do and do not utilize load-cell measurements.

Incorporating tension measurements ($j = \tau l \sigma \epsilon$) substantially improves position accuracy. For instance, using only 8 equilibrium poses, the error drops from 23 mm (trial b) to 12 mm (trial a). Similarly, for $k = 27$, it decreases from 22 mm (trial d) to 7.2 mm (trial c). This trend confirms that static equilibrium constraints and cable tension measurements significantly enhance positional accuracy. The effect on orientation accuracy is more difficult to interpret. When comparing trials a and b, the inclusion of tension measurements reduces the orientation error from 5.44° to 1.24°, showing a clear benefit. However, this trend does not persist when increasing the number of poses. In fact, trial c (tension-based) results in a worse orientation estimate (3.14°) than trial a (1.24°). This may be due to less favorable pose distribution or greater noise influence in the larger dataset. Conversely, in the kinematic-only approach, increasing k from 19 (trial b) to 128 (trial d) halves the orientation error (5.44° to 2.86°), as expected. These results suggest that the impact of the number of measurement poses on orientation accuracy is method-dependent: while the kinematic-only method benefits from more poses, the tension-based method does not exhibit a clear trend and may be sensitive to dataset-specific factors.

Overall, the tension-based method (a, c) achieves better position accuracy while requiring significantly fewer measurements than the kinematic-only method (b, d). This is particularly noteworthy because the tension-based method relies on a simplified physical model (neglecting cable sag and elasticity) and uses cable-tension measurements, which typically carry greater uncertainty than kinematic signals. Yet, despite these limitations, the inclusion of tension data and equilibrium constraints consistently improves the positional estimate. It is also important to note that, although internal statics has been previously used in self-calibration problems [14], to our knowledge, direct use of cable tension measurements for initial-pose self-calibration in *UACDPRs* is novel. This work therefore provides the first quantitative comparison of statics- vs. kinematics-based methods using real tension data. To obtain self-calibration results comparable to those reported in [23], which achieved a best-case accuracy of $\varepsilon_p = 23.36$ mm and $\varepsilon_r = 2.18°$ using a fast but manual procedure, the kinematic-only approach requires at least $k = 128$ poses and a total calibration time of over 10 minutes. In contrast, the tension-based method achieves better performance with just $k = 8$ and with the same self-calibration duration. These findings emphasize the importance of exploiting static configurations and cable-tension measurements to enable fast and accurate automatic self-calibration in *UACDPRs*.

5. Conclusions

In this paper, we presented a novel data acquisition framework for initial-pose self-calibration in *UACDPRs*. The proposed procedures support automatic and rapid data collection, extending the approach introduced in [23], which was fast but not automated. We improve upon [14], where high accuracy required prolonged acquisition durations.

The proposed approach exploits pure force joint control to guide the *EE* through static equilibrium configurations while ensuring that cable constraints remain active. By incorporating multiple sensor

measurements, including cable tensions, into the calibration process, the number of required measurement poses is significantly reduced while maintaining high accuracy in the initial-pose estimation. An experimental validation demonstrated that using static equilibrium poses in the calibration problem is mandatory to obtain accurate results in the estimation of the initial position. In particular, our analysis demonstrated that leveraging force measurements effectively reduces the number of required configurations, thus minimizing calibration time.

For future work, we aim to further automate the data acquisition process by developing a comprehensive tool that integrates automatic measurement pose selection, motion planning, and a control strategy to minimize both the path length and transition time between equilibrium poses, thus reducing unnecessary motion and overall data acquisition time. Another objective is to eliminate the need for an initial trajectory tuning phase, which currently must be repeated after each reconfiguration of the *UACDPR* and limits the system's full automation potential. Additionally, we plan to integrate the two self-calibration methods presented in this paper into a unified approach, leveraging their respective advantages: achieving high accuracy in both initial position and orientation while minimizing the required number of equilibrium poses. A key challenge in this integration will be designing an algorithm for automatic data extraction from logged measurements, ensuring that static equations are applied only when the *EE* is in equilibrium configurations, while other sampled data contributes to the kinematic formulation.

Author contributions. F. Zoffoli and E. Idà conceived and designed the study. F. Zoffoli conducted data gathering and data processing. M. Carricato provided funding for the study and experimentation. F. Zoffoli, E. Idà, and M. Carricato wrote the article.

Financial support. This study was carried out within the MICS (Made in Italy - Circular and Sustainable) Extended Partnership and received funding from the European Union Next-GenerationEU (PIANO NAZIONALE DI RIPRESA E RESILIENZA (PNRR) - MISSIONE 4 COMPONENTE 2, INVESTIMENTO 1.3 - D.D. 1551.11-10-2022, PE00000004), and thanks to the support of the Italian Ministry of University and Research (MUR) through the PRIN 2020 grant "Extending Robotic Manipulation Capabilities by Cooperative Mobile and Flexible Multi-Robot Systems (Co-MiR)" (No. 2020CMEFPK).

Competing interests. The authors declare no conflicts of interest exist.

Data availability. The complete dataset used in this study has been made publicly available in [40].

Ethical approval. Not applicable.

References

[1] Y. Hu, H. Liu and H. Yuan, "A portable cable-suspended parallel robot and its applications in indoor inspection," *IEEE Robot. Autom. Lett.* **9**(11), 10644–10651 (2024). doi: 10.1109/LRA.2024.3469819.

[2] L. Gagliardini, S. Caro, M. Gouttefarde and A. Girin, "A reconfiguration Strategy for Reconfigurable Cable-Driven Parallel Robots," **In:** *Proceedings of the 2015 IEEE International Conference on Robotics and Automation (ICRA)*, *IEEE*, (May, Seattle, WA, USA, 2015) pp. 1613–1620. 26-30 May, doi: 10.1109/ICRA.2015.7139404.

[3] L. Gagliardini, S. Caro, M. Gouttefarde and A. Girin, "Discrete reconfiguration planning for cable-driven parallel robots," *Mech. Mach. Theory* **100**, 313–337 (2016). doi: 10.1016/j.mechmachtheory.2016.02.014.

[4] D. Q. Nguyen, M. Gouttefarde, O. Company and F. Pierrot, "On the Analysis of Large-Dimension Reconfigurable Suspended Cable-Driven Parallel Robots," **In:** *Proceedings of the 2014 IEEE International Conference on Robotics and Automation (ICRA)*, *IEEE*, (Hong Kong, China, 2014) pp. 5728–5735. 31 May - 7 June. doi: 10.1109/ICRA.2014.6907701.

[5] L. Gagliardini, M. Gouttefarde and S. Caro, "Design of Reconfigurable Cable-Driven Parallel Robots, Mechatronics for Cultural Heritage and Civil Engineering, Intelligent Systems," **In:** *Control and Automation: Science and Engineering* (E. Ottaviano, A. Pelliccio and V. Gattulli, eds.), Vol. 92 (Springer, 2018) pp. 85–113. doi: 10.1007/978-3-319-68646-2_4.

[6] H. Hussein, J. C. Santos and M. Gouttefarde, "Geometric Optimization of a Large Scale CDPR Operating on a Building Facade," **In:** *Proceedings of the IEEE/RSJ International Conference on Intelligent Robots and Systems (IROS)*, (Madrid, Spain , 2018) pp. 5117–5124. 1–5 October. doi: 10.1109/IROS.2018.8593900.

[7] H. H. Cheng and D. Lau, "Cable attachment optimization for reconfigurable cable-driven parallel robots based on various workspace conditions," *IEEE Trans. Robot.* **39**(5), 3759–3775 (2023). doi: 10.1109/TRO.2023.3288838.

[8] E. Ida' and M. Carricato, "Static workspace computation for underactuated cable-driven parallel robots," *Mech. Mach. Theory* **193**, 1–19 (2024). doi: 10.1016/j.mechmachtheory.2023.105551.

[9] M. Angelini, E. Ida', D. Bertin, E. Mantovani, D. Bazzi, V. Orassi and M. Carricato, "An underactuated cable-driven parallel robot for marine automated launch and recovery operations," *J. Mech. Robot.* **17**(1), 1–10 (2024). doi: 10.1115/1.4065394.
[10] W. Khalil and E. Dombre, *Modeling Identification and Control of Robots* (CRC press, 2002) pp. 257–310.
[11] J. A. dit Sandretto, D. Daney and M. Gouttefarde, "Calibration of a Fully-Constrained Parallel Cable-Driven Robot, Romansy 19 – Robot Design, Dynamics and Control," **In:** *CISM International Centre for Mechanical Sciences* (V. Padois, P. Bidaud and O. Khatib, eds.), Vol. 544 (Springer, 2013) pp. 77–84. doi: 10.1007/978-3-7091-1379-0_10.
[12] E. Ida', S. Briot and M. Carricato, "Identification of the inertial parameters of underactuated cable-driven parallel robots," *Mech. Mach. Theory* **167**, 1–14 (2022). doi: 10.1016/j.mechmachtheory.2021.104504.
[13] C. Martin, M. Fabritius, J. T. Stoll and A. Pott, "A laser-based direct cable length measurement sensor for CDPRs," *Robotics* **10**(60), 1–11 (2021). doi: 10.3390/robotics10020060.
[14] E. Idá, J. P. Merlet and M. Carricato, "Automatic Self-Calibration of Suspended Under-Actuated Cable-Driven Parallel Robot Using Incremental Measurements, Cable-Driven Parallel Robots, CableCon 2019," **In:** *Mechanisms and Machine Science* (A. Pott and T. Bruckmann, eds.), Vol. 74 (Springer, 2019) pp. 333–344. doi: 10.1007/978-3-030-20751-9_28.
[15] S. Gabaldo, E. Ida' and M. Carricato, "Pose-Estimation Methods for Planar Underactuated Cable-Driven Parallel Robots, Cable-Driven Parallel Robots, CableCon 2023," **In:** *Mechanisms and Machine Science* (S. Caro, A. Pott and T. Bruckmann, eds.), Vol. 132 (Springer, 2023) pp. 3–15. doi: 10.1007/978-3-031-32322-5_1.
[16] S. Gabaldo, E. Ida' and M. Carricato, "Pose-estimation methods for underactuated cable-driven parallel robots," *Mech. Mach. Theory* **199**, 1–13 (2024). doi: 10.1016/j.mechmachtheory.2024.105690.
[17] J. P. Merlet, "An Experimental Investigation of Extra Measurements for Solving the Direct Kinematics of Cable-Driven Parallel Robots," **In:** *Proceedings of the 2018 IEEE International Conference on Robotics and Automation (ICRA)*, *IEEE*, (Brisbane, QLD, Australia, 2018) pp. 6947–6952. 21–25 May. doi: 10.1109/ICRA.2018.8460901.
[18] D. Lau, "Initial Length and Pose Calibration for Cable-Driven Parallel Robots with Relative Length Feedback, Cable-Driven Parallel Robots," **In:** *Mechanisms and Machine Science* (C. Gosselin, P. Cardou, T. Bruckmann and A. Pott, eds.), Vol. 53 (Springer, 2017) pp. 140–151. doi: 10.1007/978-3-319-61431-1_13.
[19] B. Wang, S. Caro and E. Point, "Initial Length and Pose Self-Calibration Method for Cable-Driven Parallel Robots," **In:** *Mechanism Design for Robotics, MEDER 2021* (S. Zeghloul, M. A. Laribi and M. Arsicault, eds.), Vol. 103 (Springer, 2021) pp. 90–101. Mechanisms and Machine Science. doi: 10.1007/978-3-030-75271-2_10.
[20] Z. Zhang, G. Xie, Z. Shao and C. Gosselin, "Kinematic calibration of cable-driven parallel robots considering the pulley kinematics," *Mech. Mach. Theory* **169**, 1–18 (2022). doi: 10.1016/j.mechmachtheory.2021.104648.
[21] R. J. Caverly, K. Bunker, S. Patel and V. L. Nguyen, "Forward Kinematics and Online Self- Calibration of Cable-Driven Parallel Robots with Covariance-Based Data Quality Assessment, Cable-Driven Parallel Robots, CableCon 2023," **In:** *Mechanisms and Machine Science* (S. Caro, A. Pott and T. Bruckmann, eds.), Vol. 132 (Springer, 2023) pp. 369–380. doi: 10.1007/978-3-031-32322-5_30.
[22] R. J. Caverly, S. K. Cheah, K. R. Bunker, S. Patel, N. Sexton and V. L. Nguyen, "Online self-calibration of cable-driven parallel robots using covariance-based data quality assessment metrics," *J. Mech. Robot.* **17**(1), 1–13 (2024). doi: 10.1115/1.4065236.
[23] F. Zoffoli, E. Ida' and M. Carricato, "A Rapid Initial-Pose Self-Calibration Method for Underactuated Cable-Driven Parallel Robots," **In:** *Advances in Italian Mechanism Science, IFToMM Italy 2024, Mechanisms and Machine Science* (G. Quaglia, G. Boschetti and G. Carbone, eds.), Vol. 163 (Springer, 2024) pp. 366–374. doi: 10.1007/978-3-031-64553-2_43.
[24] M. Fabritius, P. Miermeister, W. Kraus and A. Pott, "A framework for analyzing the accuracy, complexity, and long-term performance of cable-driven parallel robot models," *Mech. Mach. Theory* **185**, 1–18 (2023). doi: 10.1016/j.mechmachtheory.2023.105331.
[25] E. Idà, S. Briot and M. Carricato, "Natural oscillations of underactuated cable-driven parallel robots," *IEEE Access* **9**, 71660–71672 (2021). doi: 10.1109/ACCESS.2021.3071014.
[26] P. Miermeister and A. Pott, "Auto Calibration Method for Cable-Driven Parallel Robots Using Force Sensors," **In:** *Latest Advances in Robot Kinematics* (J. Lenarcic and M. Husty, eds.), (Springer, 2012) pp. 269–276. doi: 10.1007/978-94-007-4620-6_34.
[27] Z. Liu, Z. Qin, H. Gao, G. Sun, Z. Huang and Z. Deng, "Initial-pose self-calibration for redundant cable-driven parallel robot using force sensors under hybrid joint-space control," *IEEE Robot. Autom. Lett.* **8**(3), 1367–1374 (2023). doi: 10.1109/LRA.2023.3238178.
[28] E. Ida' and V. Mattioni, "Cable-driven parallel robot actuators: State of the art and novel Servo-Winch," *Actuators* **11**(10), 1–13 (2022). doi: 10.3390/act11100290.
[29] L. Guagliumi, A. Berti, E. Monti, M. Fabritius, C. Martin and M. Carricato, "Force-sensor-free implementation of a hybrid position–Force control for overconstrained cable-driven parallel robots," *Robotics* **13**(25), 1–21 (2024). doi: 10.3390/robotics13020025.
[30] A. E. Bryson and Y. C. Ho, *Applied Optimal Control: Optimization, Estimation and Control* (Taylor & Francis, 1975), pp. 349–359.
[31] J. H. Borm and C. H. Meng, "Determination of optimal measurement configurations for robot calibration based on observability measure," *Int J. Robot. Res.* **10**(1), 51–63 (1991). doi: 10.1177/027836499101000106.
[32] D. Daney, Y. Papegay and B. Madeline, "Choosing measurement poses for robot calibration with the local convergence method and tabu search," *Int. J. Robot. Res.* **24**(6), 501–508 (2005). doi: 10.1177/0278364905053185.
[33] F. Zhang, W. Shang and S. Cong, "Choosing Measurement Configurations for Kinematic Calibration of Cable-Driven Parallel Robots," **In:** *Proceedings of the 2018 3rd International Conference on Advanced Robotics and Mechatronics (ICARM)*, *IEEE*, (Singapore, Singapore, 2018) pp. 397–402. 18-20 July. doi: 10.1109/ICARM.2018.8610816.

[34] H. Wang, T. Gao, J. Kinugawa and K. Kosuge, "Finding measurement configurations for accurate robot calibration: Validation with a cable-driven robot," *IEEE Trans. Robot.* **33**(5), 1156–1169 (2017). doi: 10.1109/TRO.2017.2707562.
[35] A. Lucarini, E. Idà and M. Carricato, "Rest-to-Rest Trajectory Planning for Underactuated Cable-Driven Parallel Robots Using Input Shaping: Preliminary Results," **In:** *Cable-Driven Parallel Robots, CableCon 2025, Mechanisms and Machine Science* (D. Lau, A. Pott and T. Bruckmann, eds.), (Springer, 2025) pp. 195–206. doi: 10.1007/978-3-031-94608-0_16.
[36] H. Edelsbrunner and E. P. Mücke, "Three-dimensional alpha shapes," *ACM Trans. Graph.* **13**(1), 43–72 (1994). doi: 10.1145/174462.156635.
[37] H. Zhuang, J. W. Hanqi and W. Huang, "Optimal planning of robot calibration experiments by genetic algorithms," *J. Robotic. Syst.* **14**(10), 741–752 (1997). doi: 10.1002/(SICI)1097-4563(199710)14:10<741::AID-ROB4>3.0.CO;2-U.
[38] W. Khalil and E. Dombre, *Modeling, Identification and Control of Robots* (Butterworth-Heinemann, 2004) pp. 257–289. doi: 10.1016/B978-1-903996-66-9.X5000-3.
[39] J. Lamaury and M. Gouttefarde, "A Tension Distribution Method with Improved Computational Efficiency," **In:** *Cable-Driven Parallel Robots* (T. Bruckmann and A. Pott, eds.), (Springer, Berlin, Heidelberg, 2013) pp. 71–85. doi: 10.1007/978-3-642-31988-4_5.
[40] [dataset] E. Ida', "Data set and simulation code for "A comparative analysis of initial-pose self-calibration algorithms for underactuated cable-driven parallel robots," version v1, Submitted to "Cambridge Robotica". Zenodo, Jul. 14, 2025. 2025. doi: 10.5281/zenodo.15880529.

A. Static workspace evaluation

Following the approach described in [8], the modified inverse geometrico-static problem consists of determining the cable tensions and the *EE* orientation for a given *EE* position within the workspace, under a fixed tension distribution strategy (such as the barycentric method [39]). This leads to solving, at each point, a system of three nonlinear equations in three unknowns (namely the *EE* orientation):

$$(\boldsymbol{\Xi}_M^T \boldsymbol{\Xi}_F^{-T} - \tilde{\mathbf{s}}')\mathbf{g} + \boldsymbol{\Xi}_M^T \boldsymbol{\Xi}_F^{-T\perp}\boldsymbol{\lambda} = \mathbf{0}_{3\times 1} \tag{A1}$$

where

- $\boldsymbol{\Xi}_F^T \in \mathbb{R}^{3\times n}$ and $\boldsymbol{\Xi}_M^T \in \mathbb{R}^{3\times n}$ are the translational and rotational blocks of the structure matrix $\boldsymbol{\Xi}_I^T$;
- $\boldsymbol{\Xi}_F^{-T} \in \mathbb{R}^{n\times 3}$ is any right inverse of $\boldsymbol{\Xi}_F^T$ and $\boldsymbol{\Xi}_F^{T\perp} \in \mathbb{R}^{m\times(n-3)}$ spans the nullspace of $\boldsymbol{\Xi}_F^T$;
- $\boldsymbol{\lambda} \in \mathbb{R}^{(n-3)\times 1}$ is the array derived by the chosen tension distribution algorithm.

Then, cable tensions are obtained as:

$$\boldsymbol{\tau} = \boldsymbol{\Xi}_F^{-T}\mathbf{g} + \boldsymbol{\Xi}_F^{T\perp}\boldsymbol{\lambda}. \tag{A2}$$

If the tensions satisfy the inequality constraints

$$\tau_{min} \preceq \boldsymbol{\tau} \preceq \tau_{max} \tag{A3}$$

and the pose is statically stable, then the pose is included in the static workspace. Static stability is assessed by verifying the positiveness of the free-motion stiffness matrix $\mathbf{K}_f^{\perp}$ [25]:

$$\mathbf{K}_f^{\perp} \triangleq \boldsymbol{\Xi}^{\perp T}(\mathbf{K} + \mathbf{Q})\boldsymbol{\Xi}^{\perp} \tag{A4}$$

where $\boldsymbol{\Xi}^{\perp T} \in \mathbf{R}^{(6-n)\times 6}$ is any left nullspace basis of $\boldsymbol{\Xi}^T$ ($\boldsymbol{\Xi}^{\perp T}\boldsymbol{\Xi}^T = \mathbf{0}_{(6-n)\times n}$) and the matrices $\mathbf{K}$ and $\mathbf{Q}$ are defined as:

$$\mathbf{K} \triangleq \sum_{i=1}^{n} \tau_i \begin{bmatrix} \mathbf{T}_i & -\mathbf{T}_i\tilde{\mathbf{a}}_i' \\ \tilde{\mathbf{a}}_i'\mathbf{T}_i & -\tilde{\mathbf{a}}_i'\mathbf{T}\tilde{\mathbf{a}}_i' \end{bmatrix} + \sum_{i=1}^{n} \tau_i \begin{bmatrix} \mathbf{0}_{3\times 3} & \mathbf{0}_{3\times 3} \\ \mathbf{0}_{3\times 3} & \tilde{\mathbf{t}}_i\tilde{\mathbf{a}}_i' \end{bmatrix},$$

$$\mathbf{T}_i \triangleq \frac{\|\mathbf{u}_i \times \mathbf{n}_i\|\mathbf{w}_i\mathbf{w}_i^T}{\mathbf{u}_i \cdot (\mathbf{a}_i - \mathbf{d}_i)} + \frac{\mathbf{n}_i\mathbf{n}_i^T}{\|\boldsymbol{\rho}_i\|}, \qquad \mathbf{Q} \triangleq \begin{bmatrix} \mathbf{0}_{3\times 3} & \mathbf{0}_{3\times 3} \\ \mathbf{0}_{3\times 3} & \tilde{\mathbf{s}}'\tilde{\mathbf{g}} \end{bmatrix}. \tag{A5}$$

Cite this article: F. Zoffoli, E. Idà and M. Carricato (2025). "A comparative analysis of initial-pose self-calibration algorithms for underactuated cable-driven parallel robots", Robotica **43**, 4005–4021. https://doi.org/10.1017/S0263574725102804